

Kim, D., Tracy, S. J., Smith, R. F., Gleason, A. E., Bolme, C. A., Prakapenka, V. B., Appel, K., Speziale, S., Wicks, J. K., Berryman, E. J., Han, S. K., Schoelmerich, M. O., Lee, H. J., Nagler, B., Cunningham, E. F., Akin, M. C., Asimow, P. D., Eggert, J. H., Duffy, T. S. (2021): Femtosecond X-ray Diffraction of Laser-shocked Forsterite (Mg_2SiO_4) to 122 GPa. - Journal of Geophysical Research: Solid Earth, 126, 1, e2020JB020337.

<https://doi.org/10.1029/2020JB020337>

Femtosecond X-Ray Diffraction of Laser-Shocked Forsterite (Mg₂SiO₄) to 122 GPa

Key Points:

- The phases occurring along the Hugoniot of forsterite are identified from 19 to 122 GPa
- Between 33 and 75 GPa, forsterite and forsterite III coexist for both single-crystal and polycrystalline samples
- At higher shock stress, variable degrees of amorphization are observed with different onset stresses for polycrystals and single crystals

Supporting Information:

- Supporting Information S1











Correspondence to:

D. Kim,
donghoon@princeton.edu

Citation:

Kim, D., Tracy, S. J., Smith, R. F., Gleason, A. E., Bolme, C. A., Prakapenka, V. B., et al. (2021). Femtosecond X-ray diffraction of laser-shocked forsterite (Mg₂SiO₄) to 122 GPa. *Journal of Geophysical Research: Solid Earth*, 126, e2020JB020337. <https://doi.org/10.1029/2020JB020337>

Received 7 JUN 2020
Accepted 2 DEC 2020

Donghoon Kim¹ , Sally J. Tracy^{1,2} , Raymond F. Smith³, Arianna E. Gleason⁴, Cindy A. Bolme⁵, Vitali B. Prakapenka⁶ , Karen Appel⁷, Sergio Speziale⁸ , June K. Wicks^{1,9}, Eleanor J. Berryman^{1,10} , Sirus K. Han¹, Markus O. Schoelmerich⁷, Hae Ja Lee¹¹, Bob Nagler¹¹, Eric F. Cunningham¹¹ , Minta C. Akin³ , Paul D. Asimow¹² , Jon H. Eggert³ , and Thomas S. Duffy¹ 

¹Department of Geosciences, Princeton University, Princeton, NJ, USA, ²Now at Earth and Planets Laboratory, Carnegie Institution for Science, Washington, DC, USA, ³Lawrence Livermore National Laboratory, Livermore, CA, USA, ⁴Fundamental Physics Directorate, SLAC National Accelerator Laboratory, Menlo Park, CA, USA, ⁵Los Alamos National Laboratory, Los Alamos, NM, USA, ⁶Center for Advanced Radiation Sources, University of Chicago, Chicago, IL, USA, ⁷European XFEL, Schenefeld, Germany, ⁸GFZ German Research Centre for Geosciences, Potsdam, Germany, ⁹Now at Department of Earth & Planetary Sciences, Johns Hopkins University, Baltimore, MD, USA, ¹⁰Now at CanmetMINING, Natural Resources Canada, Ottawa, ON, Canada, ¹¹Linac Coherent Light Source, SLAC National Accelerator Laboratory, Menlo Park, CA, USA, ¹²Division of Geological and Planetary Sciences, California Institute of Technology, Pasadena, CA, USA

Abstract The response of forsterite, Mg₂SiO₄, under dynamic compression is of fundamental importance for understanding its phase transformations and high-pressure behavior. Here, we have carried out an in situ X-ray diffraction study of laser-shocked polycrystalline and single-crystal forsterite (*a*-, *b*-, and *c*-orientations) from 19 to 122 GPa using the Matter in Extreme Conditions end-station of the Linac Coherent Light Source. Under laser-based shock loading, forsterite does not transform to the high-pressure equilibrium assemblage of MgSiO₃, bridgmanite and MgO periclase, as has been suggested previously. Instead, we observe forsterite and forsterite III, a metastable polymorph of Mg₂SiO₄, coexisting in a mixed-phase region from 33 to 75 GPa for both polycrystalline and single-crystal samples. Densities inferred from X-ray diffraction data are consistent with earlier gas-gun shock data. At higher stress, the response is sample-dependent. Polycrystalline samples undergo amorphization above 79 GPa. For [010]- and [001]-oriented crystals, a mixture of crystalline and amorphous material is observed to 108 GPa, whereas the [100]-oriented forsterite adopts an unknown phase at 122 GPa. The first two sharp diffraction peaks of amorphous Mg₂SiO₄ show a similar trend with compression as those observed for MgSiO₃ in both recent static- and laser-driven shock experiments. Upon release to ambient pressure, all samples retain or revert to forsterite with evidence for amorphous material also present in some cases. This study demonstrates the utility of femtosecond free-electron laser X-ray sources for probing the temporal evolution of high-pressure silicate structures through the nanosecond-scale events of shock compression and release.

1. Introduction

Mg-rich olivine (Mg,Fe)₂SiO₄, occurs widely in igneous and metamorphic rocks, and is the dominant phase in Earth's upper mantle (Ringwood, 1991). The physical properties of liquid Mg₂SiO₄ are important for modeling partial melting of the mantle and the behavior of magma oceans (Mosenfelder et al., 2007). In addition, olivine is a common constituent of terrestrial planets (Mustard et al., 2005) and meteorites (Mason, 1963), and is also found in comets (Hanner, 1999), presolar grains (Nguyen & Zinner, 2004), and in accretion disks around young stars (van Boekel et al., 2004).

Static-compression experiments have shown that at high pressure and temperature (>1,000 K), (Mg,Fe)₂SiO₄ adopts a spinelloid structure (wadsleyite) at about ~14 GPa, and then transforms to a spinel structure (ringwoodite) at ~18 GPa (Frost, 2008). At 24 GPa, ringwoodite dissociates into (Mg,Fe)SiO₃, bridgmanite and (Mg,Fe)O, ferropericlase which are expected to be the major phases of Earth's lower mantle. These phase transitions in the (Mg,Fe)₂SiO₄ system are the primary cause of the ma-

major seismic discontinuities at 410-, 520-, and 660-km depths in the Earth's mantle (Ringwood, 1991). These discontinuities play a key role in controlling the dynamics and heat flow in the Earth's interior (Ringwood, 1991).

Metastable polymorphs of forsterite, Mg_2SiO_4 , the Mg end-member of olivine, have also been reported at high pressure. A 300-K single-crystal X-ray diffraction (XRD) study showed that forsterite (orthorhombic, $Pbnm$) transforms to forsterite II (triclinic, $P1$) and forsterite III (orthorhombic, $Cmc2_1$) at 50 and 58 GPa, respectively (Finkelstein et al., 2014) (hereafter Fo, Fo II, and Fo III). Fo III is related to the postspinel calcium titanate structure and has fully 6-coordinated silicon. It remains metastable to at least 90 GPa at ambient temperature (Finkelstein et al., 2014).

Due to the geophysical importance of Mg-rich olivine, there has been much interest in understanding its shock-compression behavior (J. M. Brown et al., 1987; Michael D. Furnish & Brown, 1986; Jackson & Ahrens, 1979; Jeanloz, 1980; Langenhorst et al., 1999; Mosenfelder et al., 2007; Newman et al., 2018; Syono et al., 1981a, 1981b; Watt & Ahrens, 1983). The Hugoniot of forsterite has been interpreted to reflect transformation to a high-pressure phase through a broad mixed-phase region that begins at about 50 GPa and is completed near 100 GPa (Mosenfelder et al., 2007). This stress is much greater than that required for transformation of olivine in static experiments, suggesting a role for kinetics on the short timescales of shock experiments. The metastable Fo III phase has been reported in recent gas-gun experiments at 44 and 73 GPa based on *in situ* XRD data (Newman et al., 2018). However, the exact natures of the mixed-phase and high-pressure phase regions are still not well understood. Upon shock compression to higher pressure, olivine is reported to melt at ~ 150 GPa on the Hugoniot (J. M. Brown et al., 1987).

The dynamic behavior of olivine is also of interest for understanding shock metamorphism generated by hypervelocity impacts on planetary bodies (Langenhorst, 2002). However, application of the results of laboratory-based shock-wave experiments to natural impact events must take into consideration the difference in timescales between the two, and therefore the possibility of nonequilibrium conditions being captured in the experiments. High-pressure olivine polymorphs have been identified in shocked meteorites and are interpreted to reflect solid–solid phase transformations or crystallization of silicate liquids (Gillet et al., 2007). Ringwoodite, for example, has been identified in chondrites and Martian meteorites (Gillet et al., 2007). Analyses of such phases have been used to explore the shock and postshock stress–temperature history of such impacts, as well as their dynamic deformation mechanisms. None of the laboratory-based shock-recovery experiments on olivine to date provide direct evidence for a phase transformation or disproportionation under shock compression (Bauer, 1979; Jeanloz, 1980; Langenhorst et al., 1999; Müller & Hornemann, 1969; Reimold & Stöffler, 1978; Shinno, 2002). The exception is the work of Syono et al. (1981a), who reported evidence for $\text{MgO} + \text{MgSiO}_3$ glass in samples recovered from Fo shocked above 80 GPa.

Constraining the behavior of olivine under dynamic loading is necessary for understanding its metastable states, transformation pathways and kinetics, structural polymorphism, and equations of state, which all play a role in interpreting geophysical phenomena. Here, we report the results of *in situ* XRD measurements on laser-shock experiments on forsterite samples covering a wide stress range.

2. Materials and Methods

2.1. Sample Preparation

Synthetic single-crystal and polycrystalline Fo (Mg_2SiO_4) samples cut into $1 \text{ mm} \times 1 \text{ mm} \times \sim 50 \text{ }\mu\text{m}$ slices were used in this study. The single-crystal samples (Roditi International, unit-cell volume $V_0 = 290.0 \text{ }\text{\AA}^3$) were cut from a $10 \times 10 \times 10 \text{ mm}^3$ cube, with the main face of each slice-oriented normal to the a -, b -, or c -axis. The fully dense, synthetic, sintered polycrystalline aggregates were from the same source as used in Newman et al. (2018) and details of the sample characterization are provided therein. The approximate mean grain size was $10 \text{ }\mu\text{m}$ and the measured unit-cell volume was $289.7(2) \text{ }\text{\AA}^3$ with a corresponding density of $3.225(3) \text{ g/cm}^3$.

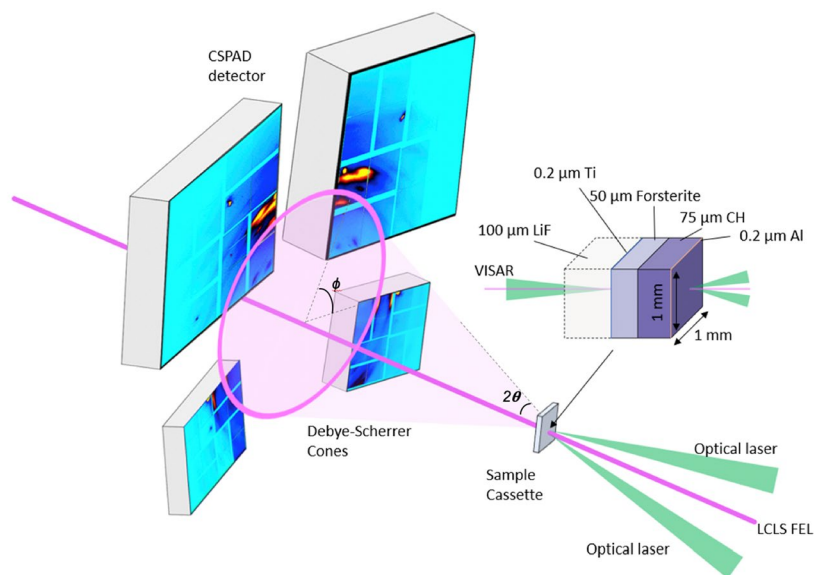


Figure 1. Schematic of the experimental setup for X-ray diffraction under laser-driven shock compression. The target package consisted of a CH ablator and a forsterite sample (with or without a LiF window). Diffraction was recorded on four CSPAD detectors. The X-rays were incident at 30° relative to target normal and drive laser beams were incident at 15° . The VISAR laser was directed normal to the rear surface of the target to measure either the Fo/LiF-interface particle velocity or the free-surface velocity. CSPAD, Cornell-SLAC Pixel Array Detectors; VISAR, velocity interferometer system for any reflector.

2.2. Laser Shock Experimental Configuration

Laser-driven shock-compression experiments were performed at the Matter in Extreme Conditions (MEC) end-station of the Linac Coherent Light Source (LCLS) at the SLAC National Accelerator Laboratory (Nagler et al., 2015). Target packages consisted of a $75\text{-}\mu\text{m}$ -thick polyimide (CH) ablator glued to an Fo sample with or without a $100\text{-}\mu\text{m}$ thick (100) LiF window epoxied to the rear surface (Figure 1). Epoxy layers were approximately $1\text{-}\mu\text{m}$ thick. The rear surface of the Fo was coated with a $0.2\text{-}\mu\text{m}$ layer of Ti to enhance the reflectivity of the sample. A $0.2\text{-}\mu\text{m}$ Al coating was deposited on the ablation side of the CH to ensure that the laser drive was optimally coupled at this interface.

Samples were shock compressed using one or both of the lasers from a two-beam 527-nm Nd:glass laser system (S. B. Brown et al., 2017) (Figure 1). The laser pulses were 10–15 ns in duration with a quasiflat-top shape (Supplemental Material, Figure S1). Experiments were performed both with and without phase plates. The shock stress was varied from 19 to 122 GPa by tuning the laser spot size ($\leq 300\text{ }\mu\text{m}$), pulse length (10–15 ns), and laser energy ($\leq 60\text{ J}$). Pulse shapes were monitored to assess the reproducibility of the drive conditions for a given laser energy, pulse length, and spot size (Table S1).

2.3. Stress Determination

The Fo free-surface or Fo/LiF-interface velocity was monitored by a line-imaging velocity interferometer system for any reflector (VISAR) with a 532-nm wavelength laser. Two independent VISAR channels with different velocity sensitivities were used to resolve ambiguities in velocity resulting from limitations in the time response of the system. The VISAR also provided information on the shock arrival time, spatial planarity, and peak elastic stress. For a given drive condition, the peak stress in a sample backed by a LiF window was determined by impedance matching using the measured interface particle velocity and the known equations of state of Fo and LiF (Figures S2 and S3 and Table S2). The error in stress was determined from propagation of uncertainties in the impedance-matching analysis. As the strength of forsterite on the Hugoniot is poorly constrained, we have not made any correction for the difference between axial stress (P_X) and mean pressure (P). Hydrodynamic simulations were performed using the one-dimensional hydrocode,

HYADES, (Larsen & Lane, 1994) to provide additional constraints of the stress evolution on compression and release (see the Supplemental Material).

2.4. In Situ X-Ray Diffraction Analysis

Samples were probed by angle-dispersive X-ray diffraction. The LCLS provided quasimonochromatic ($\Delta E/E = 0.2\%–0.5\%$), 8.5 keV, X-ray pulses of 60-fs duration, each containing 10^{12} photons. The X-rays were focused to a spot size of $\sim 20 \mu\text{m}$ at the center of the laser drive. Diffraction peaks from the sample were recorded on four Cornell-SLAC Pixel Array Detectors (CSPAD 550k) (Philipp et al., 2011), covering a two-theta (2θ) range of $15^\circ–85^\circ$ (Figure S4). For each shot, we also collected one or more preshot XRD patterns with the incident X-ray intensity attenuated by 30%–90%. This provided a precompression reference pattern and facilitated screening for strong single-crystal diffraction spots that could damage the detector. The two-dimensional (2D) CSPAD images were integrated azimuthally to convert them to one-dimensional (1D) XRD patterns. The intensity of the integrated pattern corresponding to each CSPAD was adjusted by equalizing the background from each detector. CeO_2 and LaB_6 were used as standards to calibrate the sample-to-detector distance and the orientation of each detector using the program Dioptas (Prescher & Prakapenka, 2015).

A single XRD pattern was collected during each shock-compression experiment. A time series of diffraction patterns was collected by changing the XRD probe time on a sequence of shots using the same drive conditions and nominally identical targets with and without a LiF window. The stress for the series of shots was determined from the target with a LiF window. The shock-arrival time at the LiF window or the free surface was designated as $t = 0$. XRD patterns record both the compressed and uncompressed material ahead of the shock front at time points before the shock wave reaches the LiF window or free surface ($t < 0$). In contrast, XRD patterns collected at $t > 0$ include a combination of compressed and partially released material. At time points late relative to shock propagation times, only diffraction from the released materials is recorded.

Diffraction peak assignments were initially made by comparing the observed peaks with predicted peak positions based on 300-K static data at similar pressures. Lattice d -spacings were obtained by peak fitting, and unit-cell parameters were refined by least squares fitting (Tables S3 and S4). It should be noted that some shots record only a few diffraction peaks, potentially limiting the precision of the unit-cell determination. A single-crystal analysis could not be performed due to inherent limitations of *in situ* shock-wave measurements in which only a single diffraction image is recorded per shot.

3. Results

Experiments were conducted at stresses from 19 to 122 GPa. Over this range, the shock-transit time for the 50- μm -thick Fo sample was $\sim 7–4.5$ ns. Figure 2 shows the determined stresses and calculated temperatures along with the equilibrium phase boundaries and 300-K metastable phases for Mg_2SiO_4 (Figure 2). The peak stress achieved for each sample type is listed in Table S1.

3.1. Low-Pressure Phase Regime (up to ~ 25 GPa)

Compressed forsterite was identified in XRD patterns collected from single crystals shocked to 19 ± 1 and 25 ± 1 GPa. Figure 3a shows a time series of XRD patterns for the [100]-single-crystal sample at ~ 19 GPa. Prior to the shot, we observe only diffraction from the (211) peak and, in some cases, 1–2 other forsterite peaks. Upon compression, the (211) peak is shifted to higher two-theta values, and a few additional compressed forsterite diffraction spots are observed, likely due to the single crystal breaking into a few crystallites (Figure S5). This is consistent with laboratory-based recovery experiments that report compressional fracture as a dominant deformation mechanism at these stresses (Bauer, 1979). Elongation of the spots in the azimuthal direction may reflect an increase in the mosaicity of the crystallites. There is no evidence of a phase transition at 19 GPa, consistent with gas-gun wave-profile measurements (Furnish et al., 1986). At +1.3 and +6.1 ns, the observed peaks shift to lower two-theta angles, indicating that release waves have reduced the stress. By +23.1 ns, diffraction spots, now more elongated along two-theta, are observed for multiple peaks that are all consistent with forsterite (Figures 3a and S5). The increased number of

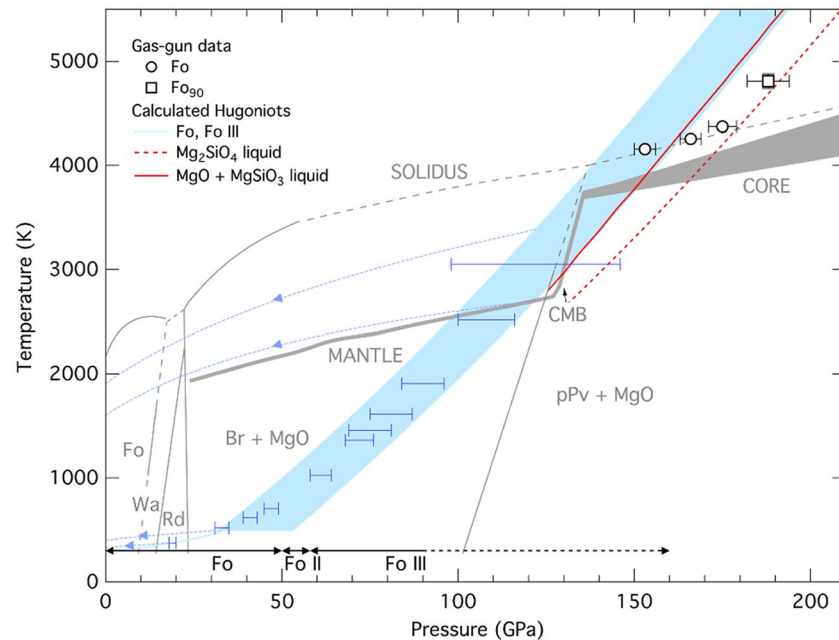


Figure 2. Phase diagram for Mg_2SiO_4 together with 300 K metastable phases (Fo II and Fo III; Finkelstein et al., 2014). Estimated Hugoniot pressure–temperature states (blue shaded region) for Fo and Fo III were calculated using the thermodynamic parameters listed in Table S6. The stresses (with uncertainty) for the present study are shown as blue lines. The light-blue dashed curves show examples of calculated release isentropes, assuming no phase change upon release. Measured shock temperatures of forsterite and olivine (Fo_{90}) from gas-gun experiments (Luo et al., 2004) are shown as open circles and a square, respectively. The gray band shows a representative geotherm for the Earth. Fo, forsterite; Wa, wadsleyite; Rd, ringwoodite; Fo II, forsterite II; Fo III, forsterite III; Br, bridgmanite; pPv, postperovskite; CMB, the core-mantle boundary. Source: Mg_2SiO_4 phase diagram (Katsura & Ito, 1989; Luo et al., 2004; Oganov & Ono, 2004; Zerr, 1998), geotherm (Stacey & Davis, 2008; Tateno et al., 2010). The red solid and dashed lines are calculated Hugoniot curves (de Koker et al., 2008).

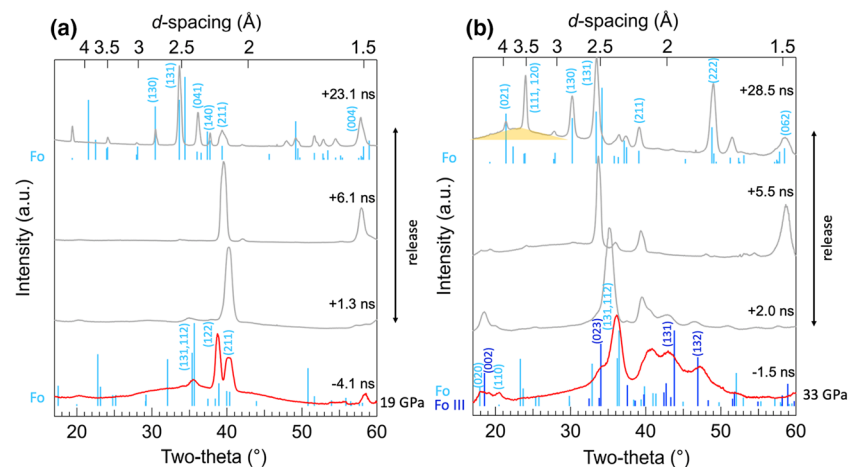


Figure 3. Integrated diffraction patterns for [100]-oriented single-crystal forsterite shots. X-ray probe times are with respect to the shock arrival at the LiF window or the free surface. That is, the reported stress corresponds to the peak Hugoniot state ($t < 0$ ns) and that times $t > 0$ represent states during which the sample is decompressing to lower stresses. (a) At a peak stress of ~19 GPa, the pattern can be indexed as forsterite (Fo) as indicated by the light blue tick marks below the pattern. (b) At 33-GPa peak stress, Fo and Fo III peaks (dark blue tick marks) are observed at probe times of -1.5 to 2.0 ns. Upon decompression from $+5.5$ to 28.5 ns, only Fo peaks and amorphous features (yellow shaded region) are observed.

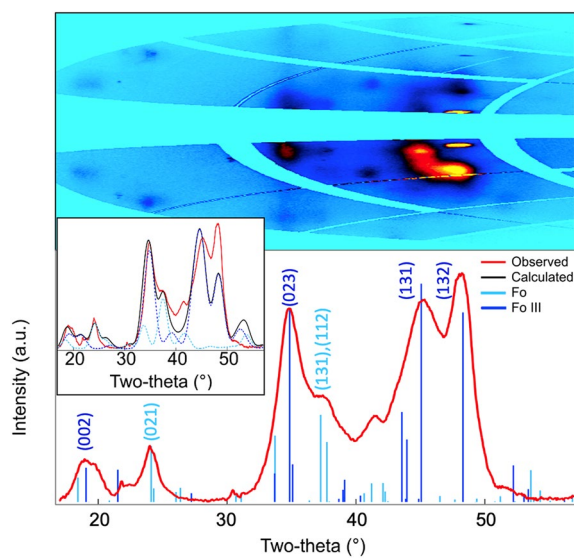


Figure 4. Background-subtracted 1D diffraction pattern (below) with CSPAD images (above) for [010]-oriented forsterite shocked to 72 GPa compared with the calculated peaks for forsterite (light blue) and forsterite III (blue). The mixed-phase assemblage can explain the observed peaks (inset) with the calculated pattern (black) for a mixture of forsterite (light blue, dashed) and forsterite III (blue, dashed).

observed diffraction spots indicates that the crystallite size is reduced, and their orientation distribution broadens especially at late times during the unloading process, likely due to fracturing resulting from interactions among the unloading waves.

3.2. Mixed-Phase Regime (33–75 GPa)

Figure 3b shows a time series of XRD patterns for forsterite shocked to a stress of 33 ± 2 GPa. Here the diffraction peaks show evidence for further fracturing and lattice strain in the crystallites (Figure S5). In addition, the observed peaks at -1.5 ns can no longer be solely assigned to forsterite. In particular, new peaks appear near a two-theta value of 34° and between 42° and 47° . We attempted to index the new peaks using the structural parameters of known high-pressure polymorphs of Mg_2SiO_4 (Smyth et al., 2000a, 2000b). Diffraction from wadsleyite, ringwoodite, or a mixture of bridgmanite and periclase cannot explain the observed patterns. Instead, we find that the metastable phases Fo II and Fo III (Finkelstein et al., 2014) can provide a reasonable match (Figure 3b). It should be noted that Fo II crystallizes in the triclinic system ($P1$, $Z = 4$) resulting in a complex diffraction pattern with many reflections. The large grain sizes maintained above the phase transition give rise to insufficient powder averaging and diffraction spots to distinguish between Fo II and Fo III. For simplicity, we have assigned the new peaks as Fo III throughout. Fo II and Fo III are both members of the postspinel family of AB_2X_4 compounds. *Ab initio* calculations suggest that only Fo III is expected to be dynamically stable (Bouibes & Zaoui, 2020; Zhang et al., 2019).

Our results are in agreement with recent in situ XRD results from gas-gun experiments, which first reported evidence for the formation of Fo III during shock loading of forsterite (Newman et al., 2018). We observe Fo III at a lower stress (~ 33 GPa) than the reported pressures of 50 and 58 GPa in 300-K static-compression experiments (Finkelstein et al., 2014) and 44 GPa in gas-gun experiments (Newman et al., 2018). Notably, *ab initio* computational studies have indicated that metastable Fo III may be able to form at as low as ~ 22 GPa (Zhang et al., 2019). These results show that the transformation from Fo to Fo III can proceed readily over timescales ranging from 10 ns (this study) to hundreds of nanoseconds (gas gun) as well as under 300-K static compression.

Shortly after the beginning of release ($+2.0$ ns), Fo III peaks are still observed, but are markedly weaker (Figure 3b). Note that times for which $t > 0$ correspond to partial or fully released states for which the stress is reduced relative to its peak value, and there may be a gradient in stress across the sample. Fo III is retained until 12 GPa on decompression at 300 K in diamond-anvil-cell experiments (Finkelstein et al., 2014). Upon unloading ($+5.5$ ns), the observed pattern can be indexed as forsterite except for a single peak near a two-theta value of 18° , which corresponds to the (002) reflection of Fo III. Hydrodynamic simulations show that stresses rapidly decrease in a few nanoseconds when release waves propagate through the sample (Figure S6). At $+28.5$ ns, all diffraction peaks can be assigned to Fo. The unit-cell volume ($V = 300 \text{ \AA}^3$) at this time is larger than that of ambient forsterite ($V = 290 \text{ \AA}^3$). In addition, a broad feature is observed over 20° – 30° two-theta (Figure S5), suggesting the possible presence of amorphous material. In static experiments, the amorphization of Fo III at ambient conditions was observed on decompression below 12 GPa (Finkelstein et al., 2014).

Fo III peaks were observed for all four types of starting materials when shock-compressed to stresses in the range of 33–75 GPa (Table S1). In experiments on an [010]-oriented crystal shocked to 40 ± 2 GPa, a mixture of compressed Fo and Fo III was observed (Figure S7). The lattice parameters of the Fo III could not be determined due to an insufficient number of observed peaks. Figure 4 shows the 2D diffraction image and corresponding integrated 1D pattern for [010] Fo shocked to 72 ± 4 GPa. The observed peaks are indexed as a mixture of Fo and Fo III. The integrated pattern is similar to that obtained from gas-gun shock-compression experiments (Newman et al., 2018) (Figure S8). However, in contrast to Newman et al. (2018), who

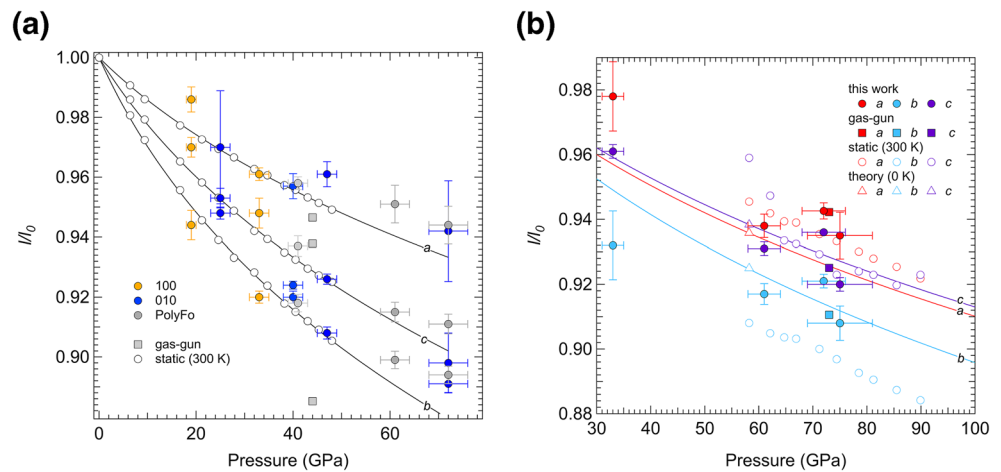


Figure 5. Relative unit-cell axial lengths of (a) forsterite and (b) forsterite III under shock and static compression. (a) Filled symbols are shock data (this study and gas-gun measurements (Newman et al., 2018)). 100 and 010 refer to the orientation of the forsterite crystals, respectively. PolyFo refers to polycrystalline forsterite. Open symbols are 300-K static-compression data (Finkelstein et al., 2014). The 300-K pressure evolution of the lattice parameters from static-compression data for forsterite are shown as black solid lines. (b) Open symbols are static (Finkelstein et al., 2014) and theoretical data (Zhang et al., 2019). The variation of Fo III lattice parameters from theoretical calculations are shown as red, purple, and light-blue solid lines. For tabular data, see Table S1. The initial values of the unit-cell parameters of Fo III come from calculations using the generalized gradient approximation method (Zhang et al., 2019).

interpreted their gas-gun XRD pattern as a complete transformation to Fo III, our interpretation is that compressed Fo and Fo III coexist at 40–44 and 72–73 GPa under both laser and gas-gun compression (Figure S8).

The 72-GPa diffraction pattern for shock-compressed [010]-forsterite shows a complex combination of broad spots and ring-like peaks (Figure 4). In this case, we observed that the single-crystal sample was altered by the X-ray beam during the preshot diffraction measurement. As shown in Figure S9, exposure of single-crystal sample to the FEL X-ray beam resulted in the appearance of multiple diffraction spots on subsequent exposure. This indicated that the single crystal disintegrated into smaller crystallites. X-ray damage due to FEL pulses has been identified in previous studies on diamond and other materials (Inoue et al., 2016; Medvedev et al., 2018).

Figure 5 shows the relative lattice parameters determined for Fo and Fo III in this study compared with previous shock (gas-gun) and static-compression data (Table S1). Although there are considerable uncertainties in the shock-wave data due to the spotty nature of the patterns as well as stress uncertainty, the lattice parameters are generally consistent with static data (Finkelstein et al., 2014; Newman et al., 2018) and *ab initio* computations (Zhang et al., 2019). Shock-induced defects and shear stresses may account for discrepancies between our data and some *ab initio* studies (Zhang et al., 2019).

3.3. High-Pressure Phase Regime (Above 79 GPa)

Although Fo III is observed at 61 ± 3 GPa for the shocked polycrystalline sample, the diffraction pattern changes when shocked to stresses between 79 ± 5 and 90 ± 6 GPa (Figure 6a). At these stresses, we observe two broad, untextured peaks, which we interpret as amorphization of the sample (see “Discussion” below). On release from these stresses, diffraction spots begin to emerge, indicating crystallization from the amorphous phase (top traces in Figure 6a). Predicted diffraction peak positions for Fo III are compared with the observed pattern in Figure S10, but neither Fo III nor Fo can explain the peak near a two-theta value of 41° – 42° . We speculate that a related postspinel structure may form on release. Several postspinel structures have been identified in AB_2X_4 compounds at high pressure (Errandonea, 2014; Yamanaka et al., 2008).

Diffraction measurements were performed for the [010] and [001] orientations at 108 ± 8 GPa (Figure 6b). In contrast to the polycrystalline material, these diffraction patterns show evidence of signif-

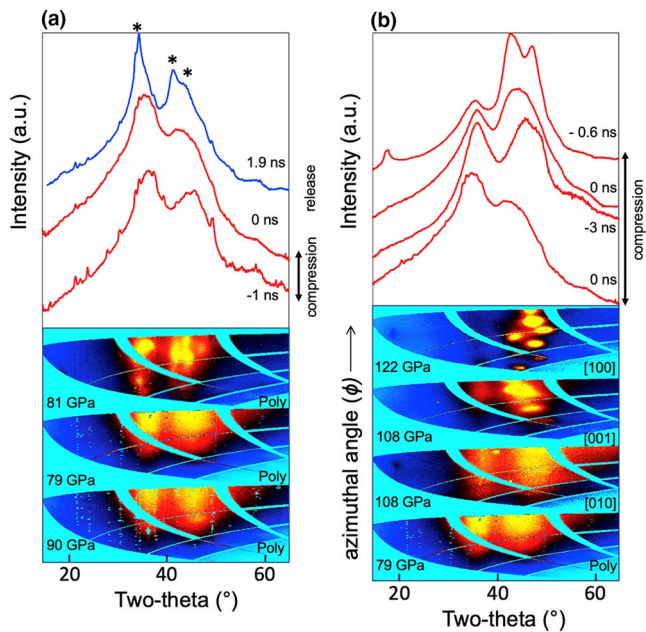


Figure 6. Integrated X-ray diffraction patterns compared with CSPAD images. (a) Time series at a peak stress of 79–90 GPa for a polycrystalline sample. The sample becomes amorphous at these stresses on compression. Diffraction peaks from the uncompressing starting material produce the small, sharp peaks on the 79- and 90 GPa spectra. These peaks are mostly masked here to more clearly show the amorphous structure. Upon release (+1.9 ns), the stress decreases from its peak value and new peaks (asterisks) appear that cannot be assigned to Fo or Fo III. (b) The degree of amorphization is highly dependent on the starting material (see the lower CSPAD images). A fully amorphous structure is observed at 79 GPa for the polycrystalline sample, whereas a partial loss of crystallinity and amorphous structure are observed for the [010] and [001] samples at 108 GPa. The [100] sample retains crystalline peaks at 122 GPa.

icant disordering, but not complete amorphization. The [001] sample retains a higher degree of crystallinity than the [010] orientation. Upon integration, the diffraction patterns for all samples are broadly similar, consisting of two broad diffraction features near 36° and 47° two-theta (Figure 6b). This suggests that there is a continuous evolution from a disordered crystal to a fully amorphous phase with an amorphization stress that depends on the sample's starting orientation.

In contrast, [100]-forsterite shocked to a peak stress of 122 ± 24 GPa retains a high degree of crystallinity as indicated by the spotty nature of the diffraction pattern (Figure 6b). In this case, the observed peaks cannot be indexed as Fo or Fo III, as neither of these phases alone nor a mixture of the two phases can explain the peak near a two-theta of 44° (~ 1.95 Å) (Figure 7). We attempted to index the peaks to other possible postspinel-type phases of Mg_2SiO_4 , but could not explain the observed peaks. High-pressure equilibrium phase assemblages such as bridgmanite and periclase or postperovskite and periclase also fail to explain the observed pattern. Therefore, [100]-Fo shocked to this stress appears to transform to an unknown high-pressure phase or a mixture of Fo III and an unknown phase.

Just after breakout (+0.2 ns), the diffraction peaks broaden as the stress begins to decrease in the sample (Figures 7 and S5c). The two shots at the same delay time show different degrees of crystallinity, which may reflect shot-to-shot variation of the sample thickness, peak stress for a particular laser setting, or a heterogeneous stress state on release (Figure S5).

Upon release at +5.2 ns, sharp Fo peaks are observed, demonstrating that the unknown phase or phase assemblage reverts to forsterite ($V = 297\text{--}300$ Å³) on decompression (Figure 7). This is consistent with our lower stress results. At +10.4 ns, two sets of closely spaced Fo diffraction peaks are observed, suggesting that the interaction of release waves produces a heterogeneous stress condition. Additionally, we observe a broad background at low two-theta, comparable to that

of Mg_2SiO_4 liquid and glass as reported by Wilding et al. (2008). This suggests that the unknown phase may have become amorphous or could be partially melted due to the residual high temperature on release (Figure 2).

4. Discussion

4.1. Wave Profiles and Peak Elastic Stress

The VISAR wave profiles provide constraints on the peak elastic stress, σ_E , of forsterite under the nanosecond timescales of laser-shock compression. The highest-quality data were obtained for the [010]-oriented single-crystal starting material, as shown in Figure S11. The measured σ_E values are 13, 18, and 26 GPa for shots corresponding to peak sample stresses of 40, 47, and 72 GPa, respectively, using the orientation-dependent $U_S\text{--}u_P$ relation in the elastic region shown in Figure S3 (Syono et al., 1981b). These values are larger than the previously reported σ_E of 12 GPa for crystals shocked along [010] to peak stresses of 15–37 GPa from gas-gun studies (Syono et al., 1981b). Our results show a strong correlation between σ_E and the peak stress, which was also not observed in the gas-gun experiments. A large increase in σ_E in high-strain-rate laser-driven compression experiments has also been reported in other materials (Smith et al., 2011; Tracy et al., 2019). None of the measured wave profiles show evidence for any additional multiwave structure that could be associated with a crystalline phase transformation or amorphization.

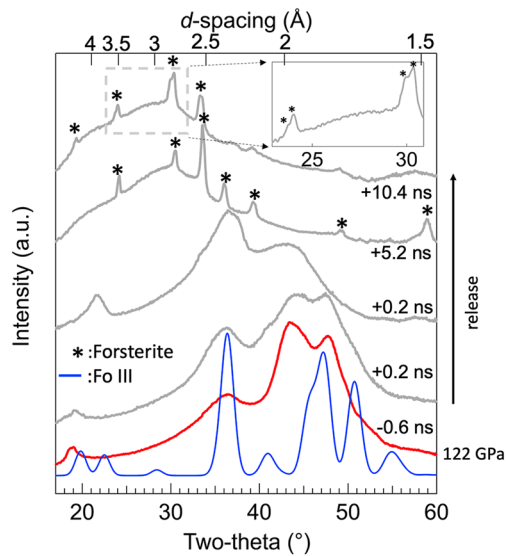


Figure 7. Integrated diffraction patterns for time series of shock compressed [100]-oriented forsterite collected at a peak stress of ~ 122 GPa for [100] single crystals. The calculated pattern for Fo III (blue) is compared with the observed data (red, gray). Asterisks indicate forsterite peaks upon stress release. The inset shows an expanded view of the region in the gray box.

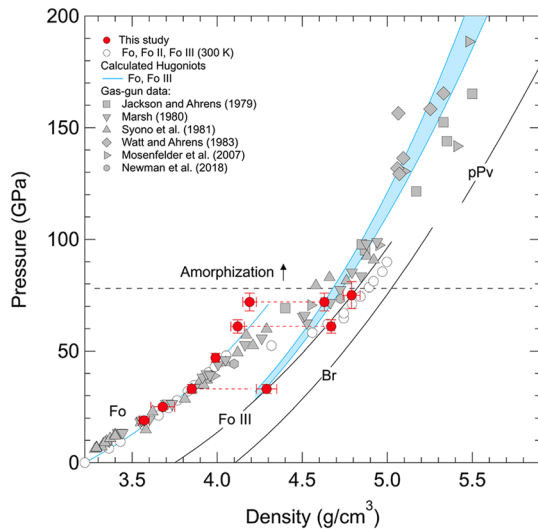


Figure 8. Densities determined from the present data (red symbols) compared with continuum gas-gun results (gray symbols) (Jackson & Ahrens, 1979; Marsh, 1980; Mosenfelder et al., 2007; Newman et al., 2018; Syono et al., 1981b; Watt & Ahrens, 1983). 300-K static compression data are shown as open symbols (Finkelstein et al., 2014). The light-blue solid line and shaded region indicate a calculated Hugoniot for Fo and Fo III based on the thermodynamic parameters in the Supplemental Material, Table S6. The densities of the two components (Fo and Fo III) in the mixed-phase region are connected by red dashed lines. The Fo III (Zhang et al., 2019), bridgmanite (Br) (Tange et al., 2012), and post perovskite (pPv) (Sakai et al., 2016) pressure–volume EOS at 300 K are shown as solid black curves.

4.2. Equation of State

A mixture of Fo and Fo III is observed on the Hugoniot from 33 to 75 GPa. Figure 8 shows densities obtained from our XRD measurements compared with those measured at the continuum level from gas-gun experiments. Beginning at 28 GPa, continuum Hugoniot states become at first slightly and then increasingly denser than forsterite at 300 K, consistent with the appearance and growth of the denser polymorph, as observed in our XRD data. Above 60 GPa, the densities of Fo III determined from our X-ray data are similar to static-compression results for this phase (Finkelstein et al., 2014). The fraction of Fo III is $\sim 50\%$ – 80% , based on a comparison of the densities derived from the XRD patterns for Fo and Fo III at 72 GPa (Figure 4) with those measured at the continuum level in gas-gun experiments at about this stress (Figure 8). This is broadly comparable to the observed relative diffraction intensities of the spotty sample, although given the large crystal size only qualitative analysis of peak intensities is possible (Figure 4).

Our results for Mg_2SiO_4 are similar to those reported recently for [100]-oriented single crystal enstatite (Mg,FeSiO_3 , under nanosecond laser shock compression where a mixture of enstatite and a dense pyroxene-like phase was observed up to 80 GPa (Hernandez et al., 2020). The dense phase is suggested to be similar to the β -post-opx phase identified in 300-K single-crystal diamond cell experiments (Finkelstein et al., 2015). Thus, both enstatite and forsterite appear to adopt a phase mixture over similar stress ranges on the Hugoniot, composed of a compressed low-pressure phase and a high-pressure phase that corresponds to the metastable phase found in low-temperature diamond cell experiments. This indicates that mafic silicates may exhibit similar behavior under shock loading and highlights the role of metastable phases along the Hugoniot at nanosecond timescales.

In light of our findings on forsterite above, we recalculated linear fits to the shock velocity (U_S)—particle velocity (u_p) relationships from gas-gun experiments using our new assignments for the low-pressure phase (LPP) and mixed-phase (MP) regimes (Figure S3). The best-fit relationships along the Fo Hugoniot are U_S (km/s) = $6.41(24) + 1.03(2)u_p$ for the LPP regime (fit to data in the range $0.71 \leq u_p \leq 1.28$ km/s corresponding to the stress range of 18–33 GPa); and U_S (km/s) = $7.06(17) + 0.64(8)u_p$ for the MP region (fit to data in the range $1.37 \leq u_p \leq 2.86$ km/s corresponding to the stress range of 35–82 GPa) (see also Table S2).

The transition stress to Fo III observed in the present work (~ 33 GPa) is lower than that observed in static studies (50 GPa for Fo II and 58 GPa for Fo III) (Finkelstein et al., 2014). This could partially be related to a sluggish reaction rate of the transition at room temperature (Zhang et al., 2019). Alternatively, large shear stresses under shock loading may play a role in driving the transition. A lowering of phase-transition pressure/stress in laser-based dynamic compression relative to static compression has been reported in other materials such as Si (McBride et al., 2019).

4.3. Amorphization

Diffraction data from silicate glasses are generally characterized by a broad peak at low values of the scattering vector, Q [$Q = 4\pi \sin\theta/\lambda$, where

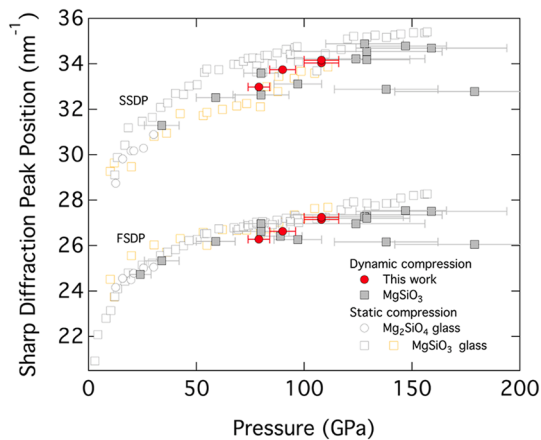


Figure 9. Position of the first (FSDP) and second (SSDP) amorphous diffraction peaks for shocked-compressed [010], [001] and polycrystalline forsterite (red circles) compared with laser-shock data for MgSiO_3 (gray squares) (Hernandez et al., 2020; Morard et al., 2020), static-compression data (open symbols) for Mg_2SiO_4 (Benmore et al., 2011), and MgSiO_3 (yellow: Kono et al., 2018; gray: Morard et al., 2020) glasses. For tabular data, see Table S5.

λ is the X-ray wavelength], known as the first sharp diffraction peak (FSDP). Under compression, a second feature (second sharp diffraction peak, SSDP) also emerges in silicate glasses. Figure 9 shows the position of the first two sharp diffraction peaks (SDPs) for amorphous Mg_2SiO_4 in our study compared to previous static and shock data for Mg_2SiO_4 and MgSiO_3 as a function of pressure. Our XRD data for shock-compressed Mg_2SiO_4 show values and trends similar to the dynamic- and static-compression data for MgSiO_3 (Table S5) (Hernandez et al., 2020; Kono et al., 2018; Morard et al., 2020) and static-compression data for Mg_2SiO_4 glass (Benmore et al., 2011). The pressure dependence of the SDP positions provides evidence of structural modifications under compression (Zeidler & Salmon, 2016). For Mg_2SiO_4 , the FSDP has been ascribed primarily to Mg–Mg and Mg–Si interactions, whereas the SSDP is associated with O–O and Mg–O interactions appearing at high pressure (Adjaoud et al., 2008; Benmore et al., 2011). The FSDP and SSDP for Mg_2SiO_4 and MgSiO_3 show a similar trend with increasing pressure. The limited Q range of our dynamic compression XRD data, however, precludes interpretation of differences in amorphous structure between Mg_2SiO_4 and MgSiO_3 along the Hugoniot.

Pressure-induced amorphization has been observed in many materials under static and dynamic compression (Hernandez et al., 2020; Sharma & Sikka, 1996; Sikka & Gupta, 1998). Our results provide evidence for

shock-induced amorphization of forsterite above 79 GPa (Figure 6). This contrasts with previous interpretations of continuum gas-gun data that suggest decomposition to crystalline periclase (MgO) and bridgmanite (MgSiO_3) (Mosenfelder et al., 2007; Syono et al., 1981a). We do not observe any diffraction attributable to MgO in samples shocked to 122 GPa, suggesting that crystallization of MgO is inhibited by the short timescales of these experiments. In dynamic-compression experiments, transformation to an equilibrium or metastable crystalline assemblage over laser ($\sim\text{ns}$) and/or gas-gun ($\sim\mu\text{s}$) timescales may be inhibited by low ionic diffusivity in the solid state (Newman et al., 2018). As a result of this kinetic limitation, a shocked sample may adopt a metastable amorphous structure as an intermediate state. It is worth noting that our results on forsterite above 80 GPa are also similar to those reported on single-crystal enstatite where amorphization is also observed at similar high stresses (>80 – 128 GPa) but below the expected melting pressure (Hernandez et al., 2020), further evidence for the corresponding behavior of enstatite and forsterite under shock loading.

Pressure-induced amorphization in silicates is often driven by shear instabilities (Richet & Gillet, 1997). The directional dependence of amorphization stress observed here may reflect differences in shear stress along the Hugoniot at high compression. Interestingly, the amorphization stress of Fo single crystals inversely correlates with their corresponding Hugoniot elastic limit (HEL) values (and shear strength) as reported by Syono et al. (1981b). The [010] orientation, which has the highest HEL, exhibits more amorphization at lower stress than the [100] orientation, which possesses the lowest HEL and does not amorphize up to 122 GPa. The presence of stress anisotropy and different orientation relationships of the crystal with respect to potential high-pressure polymorphs may lead to structural collapse at stresses that differ by several tens of GPa for different orientations of Fo crystals.

It is well known that metals can retain at least some shear strength up until melting on the Hugoniot and elastic anisotropy has been identified in aluminum single crystals shocked to 70 GPa (Choudhuri & Gupta, 2013). The degree of shear stress sustained by silicates under shock loading is less clear. Measurements of sound speeds in some silicates are consistent with bulk velocities and, hence, strengthless behavior (Grady et al., 1975). For shocked forsterite, an orientation dependence of the Hugoniot density was reported above 100 GPa (Watt & Ahrens, 1983), but this was not confirmed in subsequent experiments (Furnish & Brown, 1986). Sound-velocity measurements on shocked polycrystalline Fo and single-crystal olivine from ~ 50 to 150 GPa suggest initial release-wave speeds consistent with longitudinal sound velocities, and hence the retention of shear stiffness (J. M. Brown et al., 1987). Our results further suggest that Fo may possess

shear-stress anisotropy, leading to orientation-dependent transformation behavior, as well as differences between single crystals and low-porosity polycrystals that are retained up to 100 GPa or more.

4.4. Stress Release at Late Time

XRD patterns were recorded up to 63 ns after the start of stress release for selected samples. We consistently observe the persistence of, or the recovery of, the forsterite structure after unloading (Figures 3, 7 and S5). The diffraction patterns at these late times (~ 10 –63 ns after shock breakout) have extended Debye–Scherrer rings compared with the shock-compressed states, indicating that the crystals have broken into or recrystallized as finer-grained crystallites showing a broader distribution of orientations. At very late times, when the sample is expected to be fully released, the unit-cell volumes obtained from our diffraction data are larger than that of ambient forsterite by 2.0%, 4.5%, and 5.9% from samples shocked to peak stresses of 19, 33, and 122 GPa, respectively. This increase in volume may in part result from thermal expansion due to residual high postshock temperatures after adiabatic release.

The temperatures required to account for the observed late-time volumes following shock compression to the low stresses of 19 and 33 GPa in our experiments are about 880 and 1250 K, respectively, based on the thermal expansivity of forsterite (Kroll et al., 2012). These temperatures are significantly higher than the postshock temperatures expected along the isentropic release paths (< 500 K) (Figure 2), which should result in a volume expansion of less than 1% at 1 bar. Recent molecular dynamic simulations and shock experiments (Heighway et al., 2019) have reported that the postshock temperature of tantalum exceeds the values predicted by isentropic release. This difference is primarily explained by plastic-work heating with an additional contribution from heat released by the defects. Using a shock-physics code, Kurosawa and Genda (2018) predict that excess heating due to the effects of strength on release occurs in dunite, a rock type predominantly made of olivine. Although the strength and nature of defects in Fo on shock loading and release are not known, we speculate that similar mechanisms may be operating in our silicate samples, contributing to the larger-than-expected observed released volumes.

Alternatively, we speculate that additional lattice expansion could arise from small tensional stress states generated from the interaction of unloading waves. The spall strength of a material determines the magnitude of tension that can be dynamically sustained. A uniform tensile stress of 1–3 GPa would be sufficient to explain the observed volumes for the low-stress shots (19 and 33 GPa), considering postshock temperatures from isentropic release alone (Figure 2). The spall strength of Fo is unknown, but available measurements on minerals and rocks yield values from 0.08–1.9 GPa ($\text{SiO}_2 = 0.08$ –0.11 GPa, gabbro = 0.15 GPa, eclogite = 0.24 GPa, $\text{Al}_2\text{O}_3 = 0.5$ –0.8 GPa, and $\text{ZrO}_2 = 1.5$ –1.9 GPa) for strain rates of $\sim 10^4$ – 10^5 s $^{-1}$ in gas-gun experiments (Ai & Ahrens, 2004; Grady, 1998). In general, the spall strength increases with increasing strain rate, but decreases with increasing shock-induced temperature (Kanel et al., 1996). Strain rates in laser-driven shock experiments (10^7 – 10^9 s $^{-1}$) are 3–5 orders of magnitude higher than in plate-impact experiments, suggesting that the spall strength of Fo may be higher than the typical values measured in gas-gun experiments.

For the high-stress shot (122 GPa), the temperature required to explain the measured release volume ($V = 307 \text{ \AA}^3$) is about 1,780 K. This is within the calculated temperature range (1,590–1,910 K) expected along the isentropic-release path from the peak stress of 122 GPa (Figure 2), indicating good agreement between the measured volume and the expected release temperature. The higher temperature of these experiments may limit the material strength and thus reduce the contribution of plastic work heating or tensile stress on release. There is also evidence for possible amorphous or liquid Mg_2SiO_4 on release from this stress (Figure 7).

5. Conclusion

The phases adopted by forsterite under laser-driven shock loading to 19–122 GPa and subsequent release were determined by XRD. Our results indicate that forsterite and the metastable polymorph forsterite III coexist from ~ 33 to 75 GPa along the Hugoniot. This is generally consistent with a previous XRD study using gas-gun experiments. The lattice parameters and densities of forsterite and forsterite III under compression

determined from our shock data are consistent with values from continuum gas-gun data, as well as static-compression and gas-gun XRD studies. These results indicate that the transformation of forsterite to forsterite III can occur on timescales ranging from tens of nanoseconds (laser compression; this study) to ~microseconds (gas gun), as well as under low-temperature (300 K) static compression.

Higher stress behavior under dynamic loading depends on the initial crystal orientation. Polycrystalline forsterite undergoes amorphization above 79 GPa, but the [100]- and [001]-oriented single crystals show only partially disordered structures at 108 GPa. For the [100] orientation, an unknown crystalline phase occurs up to 122 GPa. For amorphous Mg_2SiO_4 at 79–108 GPa, two SDPs are observed, which are consistent with values for amorphous Mg_2SiO_4 and MgSiO_3 under static compression and MgSiO_3 under dynamic compression.

Upon release from high stress, we observe retention of or reversion to forsterite, with some evidence for the presence of amorphous material. The measured unit-cell volumes upon release from peak stresses of 19 and 33 GPa are larger than the 300-K values. This difference may be explained by residual shock temperatures, plastic-work heating, and/or tensile stress. In contrast to the 19- and 33-GPa decompressed unit-cell volumes, the increase in unit-cell volume upon release from 122 GPa can be explained by the expected thermal expansion caused by residual heat following isentropic release alone.

Overall, this study provides insight into the transformation of forsterite under nanosecond-duration shock loading. Future experiments are needed to better understand the effects of timescale, loading rate, and crystal orientation on kinetics, metastability, and amorphization and thereby provide better understanding of the behavior of this fundamental mineral across the timescales of laboratory and natural impact events.

Data Availability Statement

Additional experimental parameters and details of data extraction are available in the supporting information. Data from this work are archived in the Department of Geosciences community of Princeton University's DataSpace: <http://arks.princeton.edu/ark:/88435/dsp01rj4307478>.

Acknowledgments

The authors are grateful to Carol Davis from the target fabrication team at Lawrence Livermore National Laboratory (LLNL) and the staff at Matter in Extreme Conditions end-station for experimental assistance. A. M. Dillman and J. L. Mosenfelder synthesized the sintered polycrystalline samples. Gregory J. Finkelstein provided helpful comments on the manuscript. This research was supported by the U.S. Department of Energy (DE-SC0018925) and the National Science Foundation (NSF) (EAR-1644614). AEG acknowledges support from LANL Reines LDRD and the NSF Geophysics Program EAR-1446969. PDA acknowledges support from NSF Geophysics Program award EAR-1725349. M. O. Schoelmerich and K. Appel acknowledge support from the German Research Foundation DFG (AP 262/2-1 and FOR2440). This work was also performed under the auspices of the U.S. Department of Energy by LLNL under contract No. DE-AC52-07NA27344. The use of the Linac Coherent Light Source, SLAC National Accelerator Laboratory, is supported by the Department of Energy, Office of Science, Office of Fusion Energy Sciences under Contract no. DE-AC02-76SF00515.

References

- Adjaoud, O., Steinle-Neumann, G., & Jahn, S. (2008). Mg_2SiO_4 liquid under high pressure from molecular dynamics. *Chemical Geology*, 256(3–4), 185–192. <https://doi.org/10.1016/j.chemgeo.2008.06.031>
- Ai, H.-A., & Ahrens, T. J. (2004). Dynamic tensile strength of terrestrial rocks and application to impact cratering. *Meteoritics & Planetary Science*, 39(2), 233–246. <https://doi.org/10.1111/j.1945-5100.2004.tb00338.x>
- Bauer, J. F. (1979). Experimental shock metamorphism of mono- and polycrystalline olivine: A comparative study. *Proceedings of the 10th Lunar Planetary Science Conference*, pp. 2573–2596, Houston, Texas.
- Benmore, C. J., Soignard, E., Guthrie, M., Amin, S. A., Weber, J. K. R., McKiernan, K., et al. (2011). High pressure X-ray diffraction measurements on Mg_2SiO_4 glass. *Journal of Non-Crystalline Solids*, 357(14), 2632–2636. <https://doi.org/10.1016/j.jnoncrsol.2010.12.064>
- Bouibes, A., & Zaoui, A. (2020). High-pressure phase transitions of forsterite from first-principles. *Journal of Physics and Chemistry of Solids*, 136, 109161. <https://doi.org/10.1016/j.jpcs.2019.109161>
- Brown, J. M., Furnish, M. D., & McQueen, R. G. (1987). Thermodynamics for $(\text{Mg},\text{Fe})_2\text{SiO}_4$ from the Hugoniot. In M. H. Manghnani, & Y. Syono (Eds.), *High-pressure research in mineral physics* (Vol. 39, pp. 373–384). Washington, DC: American Geophysical Union. <https://doi.org/10.1029/GM039p0373>
- Brown, S. B., Hashim, A., Gleason, A., Galtier, E., Nam, I., Xing, Z., et al. (2017). Shock drive capabilities of a 30-Joule laser at the matter in extreme conditions hutch of the Linac Coherent Light Source. *Review of Scientific Instruments*, 88(10), 105113. <https://doi.org/10.1063/1.4997756>
- Choudhuri, D., & Gupta, Y. M. (2013). Shock compression of aluminum single crystals to 70 GPa: Role of crystalline anisotropy. *Journal of Applied Physics*, 114(15), 153504. <https://doi.org/10.1063/1.4824825>
- de Koker, N. P., Stixrude, L., & Karki, B. B. (2008). Thermodynamics, structure, dynamics, and freezing of Mg_2SiO_4 liquid at high pressure. *Geochimica et Cosmochimica Acta*, 72(5), 1427–1441. <https://doi.org/10.1016/j.gca.2007.12.019>
- Errandonea, D. (2014). AB2O4 compounds at high pressures. In F. J. Manjon, I. Tiginyanu, & V. Ursaki (Eds.), *Pressure-induced phase Transitions in AB2X4 chalcogenide compounds* (Vol. 189, pp. 53–73). Berlin, Heidelberg: Springer. https://doi.org/10.1007/978-3-642-40367-5_2
- Finkelstein, G. J., Dera, P. K., & Duffy, T. S. (2015). Phase transitions in orthopyroxene (En_{90}) to 49 GPa from single-crystal X-ray diffraction. *Physics of the Earth and Planetary Interiors*, 244, 78–86. <https://doi.org/10.1016/j.pepi.2014.10.009>
- Finkelstein, G. J., Dera, P. K., Jahn, S., Oganov, A. R., Holl, C. M., Meng, Y., & Duffy, T. S. (2014). Phase transitions and equation of state of forsterite to 90 GPa from single-crystal X-ray diffraction and molecular modeling. *American Mineralogist*, 99(1), 35–43. <https://doi.org/10.2138/am.2014.4526>
- Frost, D. J. (2008). The upper mantle and transition zone. *Elements*, 4(3), 171–176. <https://doi.org/10.2113/GSELEMENTS.4.3.171>
- Furnish, M. D., & Brown, J. M. (1986). Shock loading of single-crystal olivine in the 100–200 GPa range. *Journal of Geophysical Research*, 91(B5), 4723. <https://doi.org/10.1029/JB091iB05p04723>

- Furnish, M. D., Grady, D. E., & Brown, J. M. (1986). Analysis of shock wave structure in single-crystal olivine using VISAR. In Y. M. Gupta (Ed.), *Shock waves in condensed matter* (pp. 595–600). New York: North Holland.
- Gillet, P., El Goresy, A., Beck, P., & Chen, M. (2007). High-pressure mineral assemblages in shocked meteorites and shocked terrestrial rocks: Mechanisms of phase transformations and constraints to pressure and temperature histories. *Geological Society of America Special Paper*, 421, 57–82. [https://doi.org/10.1130/2007.2421\(05\)](https://doi.org/10.1130/2007.2421(05))
- Grady, D. E. (1998). Shock-wave compression of brittle solids. *Mechanics of Materials*, 29, 181–203
- Grady, D. E., Murri, W. J., & De Carli, P. S. (1975). Hugoniot sound velocities and phase transformations in two silicates. *Journal of Geophysical Research*, 80(35), 4857–4861. <https://doi.org/10.1029/JB080i035p04857>
- Hanner, M. S. (1999). The silicate material in comets. In K. Altwegg, P. Ehrenfreund, J. Geiss, & W. F. Huebner (Eds.), *Composition and origin of cometary materials* (pp. 99–108). Dordrecht: Springer Netherlands. https://doi.org/10.1007/978-94-011-4211-3_10
- Heighway, P. G., Sliwa, M., McGonagle, D., Wehrenberg, C., Bolme, C. A., Eggert, J., et al. (2019). Nonisentropic release of a shocked solid. *Physical Review Letters*, 123(24), 245501. <https://doi.org/10.1103/PhysRevLett.123.245501>
- Hernandez, J. -A., Morard, G., Guarguaglini, M., Alonso-Mori, R., Benuzzi-Mounaix, A., Bolis, R., et al. (2020). Direct observation of shock-induced disordering of enstatite below the melting temperature. *Geophysical Research Letters*, 47(15). <https://doi.org/10.1029/2020GL088887>
- Inoue, I., Inubushi, Y., Sato, T., Tono, K., Katayama, T., Kameshima, T., et al. (2016). Observation of femtosecond X-ray interactions with matter using an X-ray–X-ray pump–probe scheme. *Proceedings of the National Academy of Sciences*, 113(6), 1492–1497. <https://doi.org/10.1073/pnas.1516426113>
- Jackson, I., & Ahrens, T. J. (1979). Shock wave compression of single-crystal forsterite. *Journal of Geophysical Research*, 84(B6), 3039. <https://doi.org/10.1029/JB084iB06p03039>
- Jeanloz, R. (1980). Shock effects in olivine and implications for Hugoniot data. *Journal of Geophysical Research*, 85(B6), 3163. <https://doi.org/10.1029/JB085iB06p03163>
- Kanel, G. I., Razorenov, S. V., Bogatch, A., Utkin, A. V., Fortov, V. E., & Grady, D. E. (1996). Spall fracture properties of aluminum and magnesium at high temperatures. *Journal of Applied Physics*, 79(11), 8310–8317. <https://doi.org/10.1063/1.362542>
- Katsura, T., & Ito, E. (1989). The system Mg₂SiO₄-Fe₂SiO₄ at high pressures and temperatures: Precise determination of stabilities of olivine, modified spinel, and spinel. *Journal of Geophysical Research*, 94(B11), 15663–15670. <https://doi.org/10.1029/JB094iB11p15663>
- Kono, Y., Shibazaki, Y., Kenney-Benson, C., Wang, Y., & Shen, G. (2018). Pressure-induced structural change in MgSiO₃ glass at pressures near the Earth's core–mantle boundary. *Proceedings of the National Academy of Sciences*, 115(8), 1742–1747. <https://doi.org/10.1073/pnas.1716748115>
- Kroll, H., Kirfel, A., Heinemann, R., & Barbier, B. (2012). Volume thermal expansion and related thermophysical parameters in the Mg, Fe olivine solid-solution series. *European Journal of Mineralogy*, 24(6), 935–956. <https://doi.org/10.1127/0935-1221/2012/0024-2235>
- Kurosawa, K., & Genda, H. (2018). Effects of friction and plastic deformation in shock-comminuted damaged rocks on impact heating. *Geophysical Research Letters*, 45(2), 620–626. <https://doi.org/10.1002/2017GL076285>
- Langenhorst, F. (2002). Shock metamorphism of some minerals: Basic introduction and microstructural observations. *Bulletin of the Czech Geological Survey*, 77, 265–282.
- Langenhorst, F., Boustie, M., Migault, A., & Romain, J. P. (1999). Laser shock experiments with nanoseconds pulses: A new tool for the reproduction of shock defects in olivine. *Earth and Planetary Science Letters*, 173(3), 333–342. [https://doi.org/10.1016/S0012-821X\(99\)00224-1](https://doi.org/10.1016/S0012-821X(99)00224-1)
- Larsen, J. T., & Lane, S. M. (1994). HYADES-A plasma hydrodynamics code for dense plasma studies. *Journal of Quantitative Spectroscopy and Radiative Transfer*, 51(1–2), 179–186. [https://doi.org/10.1016/0022-4073\(94\)90078-7](https://doi.org/10.1016/0022-4073(94)90078-7)
- Luo, S.-N., Akins, J. A., Ahrens, T. J., & Asimow, P. D. (2004). Shock-compressed MgSiO₃ glass, enstatite, olivine, and quartz: Optical emission, temperatures, and melting. *Journal of Geophysical Research: Solid Earth*, 109(B5). <https://doi.org/10.1029/2003JB002860>
- Marsh, S. P. (1980). *LASL shock Hugoniot data*. Berkeley, CA: University of California Press
- Mason, B. (1963). Olivine composition in chondrites. *Geochimica et Cosmochimica Acta*, 27, 1011–1023.
- McBride, E. E., Krygier, A., Ehnes, A., Galtier, E., Harmand, M., Konôpková, Z., et al. (2019). Phase transition lowering in dynamically compressed silicon. *Nature Physics*, 15(1), 89–94. <https://doi.org/10.1038/s41567-018-0290-x>
- Medvedev, N., Tkachenko, V., Lipp, V., Li, Z., & Ziaja, B. (2018). Various damage mechanisms in carbon and silicon materials under femtosecond X-ray irradiation. *4open*, 1, 3. <https://doi.org/10.1051/fopen/2018003>
- Morard, G., Hernandez, J.-A., Guarguaglini, M., Bolis, R., Benuzzi-Mounaix, A., Vinci, T., et al. (2020). In situ X-ray diffraction of silicate liquids and glasses under dynamic and static compression to megabar pressures. *Proceedings of the National Academy of Sciences*, 117(22), 11981–11986. <https://doi.org/10.1073/pnas.1920470117>
- Mosenfelder, J. L., Asimow, P. D., & Ahrens, T. J. (2007). Thermodynamic properties of Mg₂SiO₄ liquid at ultra-high pressures from shock measurements to 200 GPa on forsterite and wadsleyite. *Journal of Geophysical Research*, 112(B6), B06208. <https://doi.org/10.1029/2006JB004364>
- Müller, W. F., & Hornemann, U. (1969). Shock-induced planar deformation structures in experimentally shock-loaded olivines and in olivines from chondritic meteorites. *Earth and Planetary Science Letters*, 7(3), 251–264. [https://doi.org/10.1016/0012-821X\(69\)90062-4](https://doi.org/10.1016/0012-821X(69)90062-4)
- Mustard, J. F., Poulet, F., Gendrin, A., Bibring, J.-P., Langevin, Y., Gondet, B., et al. (2005). Olivine and pyroxene diversity in the crust of Mars. *Science*, 307(5715), 1594–1597. <https://doi.org/10.1126/science.1109098>
- Nagler, B., Arnold, B., Bouchard, G., Boyce, R. F., Boyce, R. M., Callen, A., et al. (2015). The matter in extreme conditions instrument at the Linac Coherent Light Source. *Journal of Synchrotron Radiation*, 22(3), 520–525. <https://doi.org/10.1107/S1600577515004865>
- Newman, M. G., Kraus, R. G., Akin, M. C., Bernier, J. V., Dillman, A. M., Homel, M. A., et al. (2018). In situ observations of phase changes in shock compressed forsterite. *Geophysical Research Letters*, 45(16), 8129–8135. <https://doi.org/10.1029/2018GL077996>
- Nguyen, A. N., & Zinner, E. (2004). Discovery of ancient silicate stardust in a meteorite. *Science*, 303(5663), 1496–1499. <https://doi.org/10.1126/science.1094389>
- Oganov, A. R., & Ono, S. (2004). Theoretical and experimental evidence for a post-perovskite phase of MgSiO₃ in Earth's D'' layer. *Nature*, 430, 445–448. <https://doi.org/10.1038/nature02701>
- Philipp, H. T., Hromalik, M., Tate, M., Koerner, L., & Gruner, S. M. (2011). Pixel array detector for X-ray free electron laser experiments. *Nuclear Instruments and Methods in Physics Research Section A: Accelerators, Spectrometers, Detectors and Associated Equipment*, 649(1), 67–69. <https://doi.org/10.1016/j.nima.2010.11.189>
- Prescher, C., & Prakapenka, V. B. (2015). DIOPTAS: A program for reduction of two-dimensional X-ray diffraction data and data exploration. *High Pressure Research*, 35(3), 223–230. <https://doi.org/10.1080/08957959.2015.1059835>
- Reimold, W. U., & Stöffler, D. (1978). Experimental shock metamorphism of dunite. *Proceedings of the 9th Lunar Planetary Science Conference*, pp. 2805–2824, Houston, Texas.

- Richet, P., & Gillet, P. (1997). Pressure-induced amorphization of minerals: A review. *European Journal of Mineralogy*, 9(5), 907–934. <https://doi.org/10.1127/ejm/9/5/0907>
- Ringwood, A. E. (1991). Phase transformations and their bearing on the constitution and dynamics of the mantle. *Geochimica et Cosmochimica Acta*, 55(8), 2083–2110. [https://doi.org/10.1016/0016-7037\(91\)90090-R](https://doi.org/10.1016/0016-7037(91)90090-R)
- Sakai, T., Dekura, H., & Hirao, N. (2016). Experimental and theoretical thermal equations of state of MgSiO₃ post-perovskite at multi-megabar pressures. *Scientific Reports*, 6(1), 22652. <https://doi.org/10.1038/srep22652>
- Sharma, S. M., & Sikka, S. K. (1996). Pressure induced amorphization of materials. *Progress in Materials Science*, 40(1), 1–77. [https://doi.org/10.1016/0079-6425\(95\)00006-2](https://doi.org/10.1016/0079-6425(95)00006-2)
- Shinno, I. (2002). A Raman spectroscopic study of shocked forsterite. *Journal of Mineralogical and Petrological Sciences*, 97(4), 153–160. <https://doi.org/10.2465/jmps.97.153>
- Sikka, S. K., & Gupta, S. C. (1998). Shock induced amorphization of materials. *AIP Conference Proceedings*, 429, 145–150
- Smith, R. F., Eggert, J. H., Rudd, R. E., Swift, D. C., Bolme, C. A., & Collins, G. W. (2011). High strain-rate plastic flow in Al and Fe. *Journal of Applied Physics*, 110(12), 123515. <https://doi.org/10.1063/1.3670001>
- Smyth, J. R., Jacobsen, S. D., & Hazen, R. M. (2000a). Comparative crystal chemistry of dense oxide minerals. *Reviews in Mineralogy and Geochemistry*, 41(1), 157–186. <https://doi.org/10.2138/rmg.2000.41.6>
- Smyth, J. R., Jacobsen, S. D., & Hazen, R. M. (2000b). Comparative crystal chemistry of orthosilicate minerals. *Reviews in Mineralogy and Geochemistry*, 41(1), 187–209. <https://doi.org/10.2138/rmg.2000.41.7>
- Stacey, F. D., & Davis, P. M. (2008). *Physics of the Earth* (4th ed.). Cambridge: Cambridge University Press.
- Syono, Y., Goto, T., Sato, J., & Takei, H. (1981a). Shock compression measurements of single-crystal forsterite in the pressure range 15–93 GPa. *Journal of Geophysical Research*, 86(B7), 6181–6186. <https://doi.org/10.1029/JB086iB07p06181>
- Syono, Y., Goto, T., Takei, H., Tokonami, M., & Nobugai, K. (1981b). Association reaction in forsterite under shock compression. *Science*, 214(4517), 177. <https://doi.org/10.1126/science.214.4517.177>
- Tange, Y., Kuwayama, Y., Irifune, T., Funakoshi, K., & Ohishi, Y. (2012). P-V-T equation of state of MgSiO₃ perovskite based on the MgO pressure scale: A comprehensive reference for mineralogy of the lower mantle. *Journal of Geophysical Research*, 117(B6), B06201. <https://doi.org/10.1029/2011JB008988>
- Tateno, S., Hirose, K., Ohishi, Y., & Tatsumi, Y. (2010). The structure of iron in Earth's inner core. *Science*, 330(6002), 359–361. <https://doi.org/10.1126/science.1194662>
- Tracy, S. J., Smith, R. F., Wicks, J. K., Fratanduono, D. E., Gleason, A. E., Bolme, C. A., et al. (2019). In situ observation of a phase transition in silicon carbide under shock compression using pulsed X-ray diffraction. *Physical Review B*, 99(21), 214106. <https://doi.org/10.1103/PhysRevB.99.214106>
- van Boekel, R., Min, M., Leinert, C., Waters, L. B. F. M., Richichi, A., Chesneau, O., et al. (2004). The building blocks of planets within the 'terrestrial' region of protoplanetary disks. *Nature*, 432(7016), 479–482. <https://doi.org/10.1038/nature03088>
- Watt, J. P., & Ahrens, T. J. (1983). Shock compression of single-crystal forsterite. *Journal of Geophysical Research*, 88(B11), 9500–9512. <https://doi.org/10.1029/JB088iB11p09500>
- Wilding, M. C., Benmore, C. J., & Weber, J. K. R. (2008). In situ diffraction studies of magnesium silicate liquids. *Journal of Materials Science*, 43(14), 4707–4713. <https://doi.org/10.1007/s10853-007-2356-5>
- Yamanaka, T., Uchida, A., & Nakamoto, Y. (2008). Structural transition of post-spinel phases CaMn₂O₄, CaFe₂O₄, and CaTi₂O₄ under high pressures up to 80 GPa. *American Mineralogist*, 93(11–12), 1874–1881. <https://doi.org/10.2138/am.2008.2934>
- Zeidler, A., & Salmon, P. S. (2016). Pressure-driven transformation of the ordering in amorphous network-forming materials. *Physical Review B*, 93(21), 214204. <https://doi.org/10.1103/PhysRevB.93.214204>
- Zerr, A. (1998). Solidus of Earth's deep mantle. *Science*, 281(5374), 243–246. <https://doi.org/10.1126/science.281.5374.243>
- Zhang, Y., Zhang, Y., Liu, Y., & Liu, X. (2019). A metastable Fo-III wedge in cold slabs subducted to the lower part of the mantle transition zone: A hypothesis based on first-principles simulations. *Minerals*, 9(3), 186. <https://doi.org/10.3390/min9030186>